Article

Integrated 3D Range Camera Self-Calibration

PATRICK WESTFELD & HANS-GERD MAAS, Dresden

Summary: An integrated bundle adjustment has been developed to facilitate the precise definition of the geometry of time-of-flight range imaging cameras, including the estimation of range-measurement-specific correction parameters modelling linear, periodic and sensor-position-dependent effects of a distance measurement. The integrated calibration routine jointly adjusts data from both information channels (amplitude and range) and automatically estimates optimum observation weights. The method is based on the flexible principle of self-calibration. It does not require spatial object data, thus avoiding the time-consuming determination of reference distances with superior accuracy. The accuracy analyses carried out using a PMD[vision]® CamCube 2.0 confirm the correctness of the proposed functional contexts, but they also exhibit challenges caused by non-parameterised range-measurement-specific errors. The level of accuracy of the observations is computed by variance component estimation and becomes in mean $^{1}/_{35}$ pixel for an amplitude image coordinate measurement and 9.5 mm for a distance measurement. The precision of a 3D point coordinate can be set at 5 mm after calibration, compared to several centimetres before applying any correction terms. In the case of depth imaging technology, which is influenced by a variety of noise sources, this accuracy level is very promising.

Zusammenfassung: *Integrierte Selbstkalibrierung distanzmessender 3D-Kameras.* Die entwickelte integrierte Bündelblockausgleichung ermöglicht die Bestimmung der exakten Aufnahmegeometrie distanzmessender 3D-Kameras sowie die Schätzung distanzmessspezifischer Korrekturparameter zur Modellierung linearer, periodischer und sensorpositionsabhängiger Fehleranteile einer Streckenmessung. Die integrierte Kalibrierroutine gleicht in beiden Informationskanälen (Amplitude und Distanz in jedem Pixel) gemessene Größen gemeinsam aus und bestimmt dabei simultan optimale Beobachtungsgewichte. Die Methode basiert auf dem flexiblen Prinzip der Selbstkalibrierung und benötigt keine Objektrauminformation, wodurch insbesondere die aufwändige Ermittlung von Referenzmaßen übergeordneter Genauigkeit entfällt. Die am Beispiel des PMD[vision]® CamCube 2.0 durchgeführten Genauigkeitsuntersuchungen bestätigen die Richtigkeit der aufgestellten funktionalen Zusammenhänge, zeigen aber auch Schwächen aufgrund noch nicht parametrisierter distanzmessspezifischer Fehler. Die durch eine Varianzkomponentenschätzung festgelegten Genauigkeitsniveaus der ursprünglichen Beobachtungen betragen im Mittel $^{1}/_{35}$ Pixel für die Amplitudenbildkoordinatenmessung und 9,5 mm für die Streckenmessung. Die Qualität der 3D-Neupunktkoordinaten kann nach einer Kalibrierung mit 5 mm angegeben werden. Im Vergleich bewegt sich diese ohne Anbringen von Korrekturtermen im Bereich einiger Zentimeter. Für die durch eine Vielzahl von meist simultan auftretenden Rauschquellen beeinflusste Tiefenbildtechnologie ist dieser Genauigkeitswert sehr vielversprechend.

1 Introduction

Modulation techniques enable range cameras based on photonic mixer devices or similar principles to simultaneously produce both an amplitude image and a range image. Though monoscopic sensors, they deliver spatially resolved surface data at video rate without the need for stereo image matching, thus coming with the advantage of a considerable reduction in complexity and computing time.

The use of range cameras as measuring devices requires the modelling of deviations from the ideal projection model. As a result of its inherent design and measurement principle, range cameras simultaneously provide amplitude and range data reconstructed from one measurement signal. The simultaneous integration of all data obtained using a range camera into an integrated calibration approach is a logical consequence and represents the focus of this contribution. On the one hand, the complementary characteristics of the observations allow them to support each other due to the creation of a functional context for the measurement channels. On the other hand, the expansion of the stochastic model to include variance component estimation ensures that the heterogeneous information pool is fully exploited. An increase in accuracy and reliability can be expected by both.

The time-of-flight range imaging principle is introduced in section 2, including the sensor device, the measurement principle and the mathematical fundamentals of the range imaging process. Range cameras are subject to a variety of error sources, which affect both the optical imaging process itself and the distance measurement. Their origin and effects as well as different calibration strategies for correction are treated in section 3. The integrated self-calibrating bundle adjustment approach presented here and the results achieved are described in detail in sections 4 and 5. Finally, the work is summarised and an outlook is given in section 6.

2   Sensor

Time-of-flight range imaging cameras (ToF, RIM, 3D camera; Schwarte et al. 1999) are monoscopic digital cameras. They acquire amplitude and range images simultaneously. An active illumination unit emits modulated near infrared light, which is backscattered from the object surface to the camera. The solid-state sensor array mounted is a photonic mixer device built in CCD/CMOS technology (PMD, Spirig et al. 1995, Schwarte 1996). At each detector pixel, a distance-based charge carrier separation is performed. This demodulation delivers the phase difference between the emitted and the received signals, and consequently the range from the camera's projection centre to the target. Furthermore, amplitude information as a measure for i.a. the reflectivity of the corresponding surface points can be obtained.

In the field of RIM sensor technology, ToF-based cameras are currently available with a sensor size of up to 40,000 pixels. Each pixel thus becomes an electro-optical distance-measuring device. Low-cost, compact range cameras combine the practicality of a digital camera with the 3D data acquisition potential of conventional surface measurement systems. Thus, they represent an interesting alternative for many applications such as mobile robotics (Schulze 2010, Mönnich et al. 2011), human-machine-interaction (Kolb et al. 2010), automotive (Ringbeck et al. 2007, Reich 2011), or human motion analysis (Westfeld & Hempel 2008, Westfeld et al. 2013).

The imaging geometry of a range camera is similar to a conventional 2D camera (Fig. 1). The collinearity equations map an object point $\mathbf{X}(X,Y,Z)$ to an image point $\mathbf{x}'(x',y')$ using a central projection:

$$x'=x'_0$$
$$-c \cdot \frac{r_{11} \cdot (X-X_0)+r_{21} \cdot (Y-Y_0)+r_{31} \cdot (Z-Z_0)}{r_{13} \cdot (X-X_0)+r_{23} \cdot (Y-Y_0)+r_{33} \cdot (Z-Z_0)}$$
$$+\Delta x'$$

$$y'=y'_0$$
$$-c \cdot \frac{r_{12} \cdot (X-X_0)+r_{22} \cdot (Y-Y_0)+r_{32} \cdot (Z-Z_0)}{r_{13} \cdot (X-X_0)+r_{23} \cdot (Y-Y_0)+r_{33} \cdot (Z-Z_0)}$$
$$+\Delta y'$$

(1)

where

c: Focal length
$\mathbf{x}'_0$:   Principal point
$\Delta x'$:   Correction functions
$\mathbf{X}_0$:   Projection centre
$r_{r,c}$:   Elements of a rotation matrix $\mathbf{R}$

In addition to amplitude information, range values D are stored in each pixel location. Due to this fact, the inverse mapping, i.e. the projection of an image point into object space, is uniquely defined and can be described by:

$$\mathbf{X} = \mathbf{X_0} + (D - \Delta D) \cdot \begin{pmatrix} r_{11} & r_{12} & r_{13} \\ r_{21} & r_{22} & r_{23} \\ r_{31} & r_{32} & r_{33} \end{pmatrix} \cdot \frac{\boldsymbol{\xi}'}{\|\boldsymbol{\xi}'\|} \qquad (2)$$

where

$$\boldsymbol{\xi}' = \begin{pmatrix} x' - x'_0 - \Delta x' \\ y' - y'_0 - \Delta y' \\ -c \end{pmatrix} .$$

$\Delta \mathbf{x}' (\Delta x', \Delta y') = f(A_1, A_2, A_3, B_1, B_2, C_1, C_2)$ describes functions for the correction of imaging errors. The additional parameters implemented compensate radial $(A_1 - A_3)$ and tangential (B_1, B_2) distortions using the well-established model from (Brown 1971) as well as affinity and shear effects (C_1, C_2; El-Hakim 1986). The distance correction term ΔD should consider systematic errors in the range measurements (section 3).
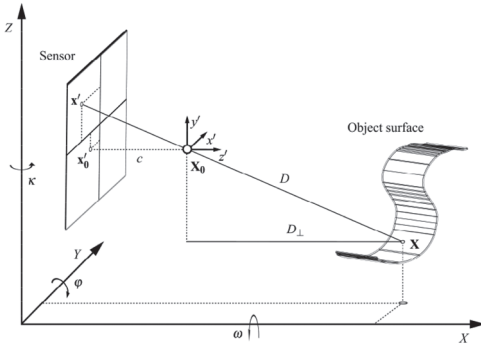

Fig. 1: Imaging geometry.

3   Error Sources and Calibration Strategies

Range cameras use standard optics for imaging. Thus, the measurement geometry corresponds to a central projection (section 2), and any deviations from the ideal model have to be compensated. Photogrammetric camera calibration techniques are employed to determine actual values for the focal length c and the principal point $\mathbf{x}'_0$ as well as for the parameters describing lens distortion and other errors, summarised in $\Delta \mathbf{x}'$.

The results of the distance measurements are also affected by a number of error sourc-

es: Effects caused by temperature and running-in behaviour or multipath propagation can be decreased or even avoided by an adequate measurement setup. Fixed pattern noise (FPN) specifies a constant distance measurement error at each pixel location and is caused by inhomogeneous CMOS material properties (Jähne 2002). Look-up tables or multiple signal sampling implemented by range camera manufacturers are used to compensate FPN effects in real-time (Luan 2001). ToF cameras acquire four raw measurements successively in order to calculate one phase image. Any sensor or object movement occurring between those sampling steps leads to motion artefacts due to phase changes (e.g. Lindner & Kolb 2009). Current range camera devices can suppress motion blur on-chip (Ringbeck & Hagebeuker 2007). Scattering (lens flare) describes the internal propagation of the incident light over the PMD array caused by signal reflections between optical filter, lens and sensor. Approaches to model the superimposition of focused light with scattered portions by point spread functions are for example given in Mure-Dubois & Hügli (2007) or Karel et al. (2012). Lichti et al. (2012) propose an empirical parameterised model to compensate for scattering-induced range errors, which is only valid under specific scene conditions. A linear distance correction term considers a shift d_0 of the measurement origin, the latter being defined to coincide with the projection centre (Fig. 2), and a scale variation d_1 caused by modulation frequency deviations:

$$\Delta D_{lin} = d_0 + d_1 D \qquad (3)$$

The modulation of the measurement signal can be influenced by harmonic interferences. A periodic distance correction term approximates the resulting cyclic phase errors (e.g. Lichti et al. 2010). The wavelengths e.g. of two sinusoidal functions with d_3 and d_5 as amplitudes correspond to ¼ and ⅛ of a constant modulation wavelength λ; phase shifts are considered by the cosine parts with d_2 and d_4 as amplitudes:

$$\Delta D_{cyc} = d_2 \cos\left(4\frac{2\pi}{\lambda}D\right) + d_3 \sin\left(4\frac{2\pi}{\lambda}D\right)$$
$$+ d_4 \cos\left(8\frac{2\pi}{\lambda}D\right) + d_5 \sin\left(8\frac{2\pi}{\lambda}D\right) \qquad (4)$$

Phase shifts can occur due to delays in signal propagation (Fuchs & Hirzinger 2008) or high viewing angles (Böhm & Pattinson 2010). A linear function of the radial distance r' using a factor d_6 can be introduced to correct a distance measurement with respect to the position on the sensor:

$$\Delta D_{x'y'} = d_6 r'$$
$$= d_6 \sqrt{\left(x' - x'_0 - \Delta x'\right)^2 + \left(y' - y'_0 - \Delta y'\right)^2}$$
(5)

The amplitude demodulated at each sensor site is a measure for the total amount of incident light. Karel & Pfeifer (2009) show that a measured distance increases with decreasing reflectivity and model the influence of the amplitude A on the ranging system by a hyperbola with parameters $d_7 - d_9$:

$$\Delta D_{amp} = -\frac{d_7}{d_8} A + \sqrt{\frac{d_7^2}{d_8^2} A^2 - 2\frac{d_9}{d_8} A + \frac{1}{d_8}}$$
(6)

Several calibration strategies are reported in literature to correct the errors described above. Depending on the observations used, they can be categorized as photogrammetric, sequential and simultaneous methods (Westfeld 2012). A classical photogrammetric test field calibration only determines the interior orientation parameters from amplitude images, e.g. Reulke (2006), Westfeld (2007), Beder & Koch (2008). Sequential approaches go one step further and calibrate the distance measurement after photogrammetric calibration. The required reference is derived from interferometric comparator displacement measurements (Kahlmann et al. 2006), precise external positioning systems, e.g. a robot (Fuchs & Hirzinger 2008), or optical tracking systems like a laser scanner (Chiabrando et al. 2009). Reference values can also be provided indirectly by the network geometry determined in the course of the self-calibration (Karel 2008, Robbins et al. 2009, Böhm & Pattinson 2010), a procedure which reduces time and instrumental effort significantly. A logical extension of the 2-step calibration is the simultaneous determination of all calibration parameters in one integrated self-calibrating bundle adjustment approach. Initial thoughts about the combination of heterogeneous ToF camera observations in one adjustment procedure were published in Westfeld (2007). Westfeld et al. (2009) move a small reference body with white spherical signals through the measurement volume of a range camera. Interior camera orientation parameters and distance calibration terms are estimated within a test-field-calibrating bundle adjustment with fixed object point coordinates. Variance component estimation ensures that the heterogeneous information pool is fully exploited. However, the experimental effort of this study was still high, because the central points of the spheres have to be determined at each position of the calibration body. Lichti et al. (2010) and Lichti & Qi (2012) perform a geometric calibration of range cameras by means of an integrated self-calibrating bundle adjustment from measurements of an 8 m² planar target field, signalised with circles. The centres of the targets in the amplitude images are measured by ellipse fitting, the corresponding range measurements must be derived from the neighbourhood by bilinear interpolation. Due to the special characteristics of the experimental setup, the distance correction model does not comprise a scale error term. Lichti et al. (2012) extend the approach to compensate the scattering bias using a specific two-plane target.

4 Integrated Self-calibrating Bundle Adjustment

4.1 *Principle*

With respect to the calibration strategies reviewed in section 3, the integrated bundle adjustment approach presented here should hold the following properties: 1) The primary aim is to simultaneously integrate all range camera information in one joint functional and stochastic context. 2) To reduce efforts in time and instrumental resources, the method is based on self-calibration. 3) If possible, the observations should not be interpolated. 4) The target field is stable, compact, portable as well as easy in set-up and dismantle.
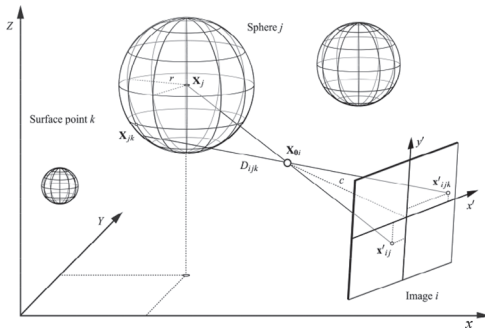
Fig. 2: Geometric model: For each range camera image i, a sphere j is projected onto the image plane. For each surface point k, amplitude information gv_{ijk} and range value D_{ijk} are stored at $(x',y')_{ijk}$.

The geometric principle of the calibration approach is shown in Fig. 2. Spheres serve as 3D reference objects. Their centres can be measured easily in the amplitude images, but the corresponding slant range measurements cannot be derived directly from range images. In order to set the geometric relation between both observation channels and to avoid range value interpolation, spheres are modelled by their surface points. Thus, the geometric model is based on the collinearity of the centre coordinates x'_{ij} of a sphere j observed in image i, the projection centre X_{0i} and the corresponding object point X_j. In addition, the integer image positions x'_{ijk} and the stored slant ranges D_{ijk} of all sphere surface points k are used. So the geometric model for distances is based on the intersection points X_{jk} of the projection rays with the surface of a sphere.

4.2 Functional Model

Amplitude Channel

The centre coordinates of the reference spheres projected onto the sensor can be measured with sub-pixel accuracy in each amplitude image by 2D least squares template matching (LSM), e.g. ACKERMANN (1984), GRÜN (1985). The template is generated automatically prior to the image matching process with respect to the amplitude gradient and the dimension of the relevant sphere (Figs. 3a and 3b). 2D LSM is parameterised by two shifts in row and column and one scale only. The approximate values originate from an algorithm for automatic image point detection based on edge detection, thresholding and connectivity analysis (BURKHART 2007). Furthermore, a student test has been implemented for testing the LSM parameters' level of significance. The mean standard deviation of the image point coordinates is $1/25$ pixel (Fig. 3c).

The image points x'_{ij}, measured in amplitude images i, form the first type of observa-

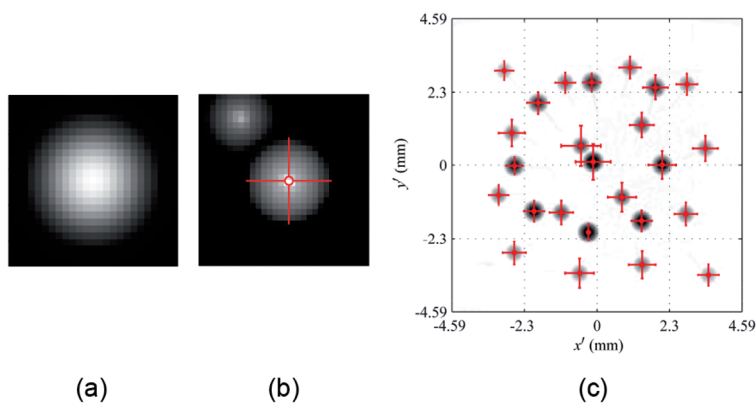(a)   (b)   (c)

Fig. 3: Amplitude image point measurement by 2D LSM. (a) Synthetically generated reference image. (b) Search image with centre cross. (c) Exemplary plot of the a-posteriori standard deviations of the translation parameters based on a single inverse amplitude image. Averaged over all images, the deviations are $1/25$ pixel or 1.70 µm with a sensor size of 9.18 mm × 9.18 mm (exaggeration: 200).

tion introduced into the bundle adjustment. On the basis of the collinearity equations (1), two observation equations $\Phi^{Ax'}$ and $\Phi^{Ay'}$ can be formulated per target j:

$$x'_{ij} =$$
$$\Phi_{ij}^{Ax'}\left(X_{0i},Y_{0i},Z_{0i},\omega_i,\varphi_i,\kappa_i,x'_0,c,\Delta x',X_j,Y_j,Z_j\right)$$
$$y'_{ij} =$$
$$\Phi_{ij}^{Ay'}\left(X_{0i},Y_{0i},Z_{0i},\omega_i,\varphi_i,\kappa_i,y'_0,c,\Delta y',X_j,Y_j,Z_j\right)$$
$$(7)$$

Range Channel

A range measurement is performed at each detector site. Thus, and in contrast to the amplitude image point measurements, ToF cameras deliver those observations directly for each sensor element. The distances measured between camera optics and sphere surfaces serve as the second observation type. The task is to automate the segmentation of the observed range values for each sphere.

The centre coordinates obtained from 2D LSM are used to localize the spheres in amplitude and range images. One patch applied to both amplitude and range image is cut out centred at the location of the target determined in the amplitude image, with the patch size depending on the sphere distance. All pixels within this patch are considered to be possible candidates for points on the sphere (Fig. 4a). In the next step, an amplitude threshold dynamically derived by fitting a Gaussian to the histogram of the amplitude image

is applied (Fig. 4b). Starting in the centre of the range patch, a radial profile analysis based on neighbouring range value differences is performed for further patch containment (Fig. 4c). A range threshold, which originates from the profile analysis, is applied afterwards (Fig. 4d). RANSAC (random sample consensus, FISCHLER & BOLLES 1981) is used to estimate the parameters of a sphere in order to eliminate gross errors, primarily caused by oversaturation or multi-path effects at object boundaries, and finally calculates the initial set of observations (Fig. 4e). In this process, the probability of a randomly selected data item being part of a sphere model is 99 %. The error tolerance for establishing the sphere model compatibility is equal to the known sphere radius. After segmentation and with respect to the experimental setup described in section 5.1, one sphere surface is on average represented by 100 points (min.: 11, max.: 261). A detailed description of the segmentation workflow is given in WESTFELD (2012).

The surface points $\mathbf{X}_{jk}$ of a sphere j, with centre $\mathbf{X}_j$ and radius r, have been segmented from ToF images i. They satisfy the following general equation of a sphere:

$$0 = \left(X_{jk}-X_j\right)^2 + \left(Y_{jk}-Y_j\right)^2 + \left(Z_{jk}-Z_j\right)^2 - r^2$$
$$(8)$$

Substituting $\mathbf{X}_{jk}$ in (8) by the right hand side of (2) geometrically corresponds to a spatial intersection of a projection ray with the surface of the sphere:
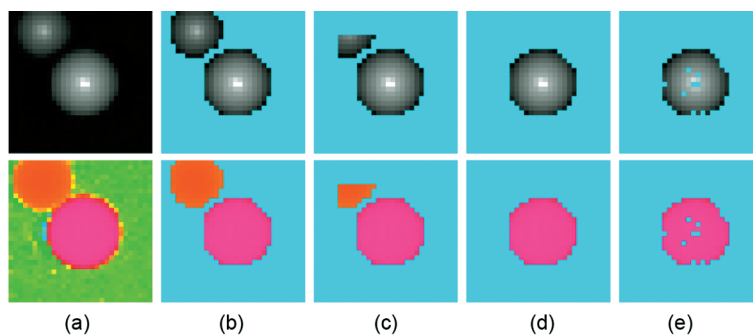

Fig. 4: Sphere segmentation stages in amplitude images (top) and colour-coded range images (bottom). Non-valid pixels are coloured in Cyan, (a) rough localization, (b) histogram analysis in amplitude image, (c) profile analysis in range image, (d) thresholding in range image, (e) Inliers of the RANSAC procedure.

$$0 = \left[X_{0i} - X_j + \left(D + \Delta D\right)_{ijk} \cdot \left(r_{11i}\xi'_{1ijk} + r_{12i}\xi'_{2ijk} + r_{13i}\xi'_{3ijk} \right) \right]^2$$

$$+ \left[Y_{0i} - Y_j + \left(D + \Delta D\right)_{ijk} \cdot \left(r_{21i}\xi'_{1ijk} + r_{22i}\xi'_{2ijk} + r_{23i}\xi'_{3ijk} \right) \right]^2 \tag{9}$$

$$+ \left[Z_{0i} - Z_j + \left(D + \Delta D\right)_{ijk} \cdot \left(r_{31i}\xi'_{1ijk} + r_{32i}\xi'_{2ijk} + r_{33i}\xi'_{3ijk} \right) \right]^2 - r^2$$

Finally, (9) is solved for D and introduced as observation equation into the bundle adjustment.

Additional Constraints

A 3D rotation can be described by three Euler angles (ω,φ,κ) or, in order to avoid ambiguous trigonometric functions, by four quaternions (q_1,q_2,q_3,q_4). The use of quaternions makes sense from a numerical point of view but requires one additional equation per camera position i to enforce an orthogonal rotation matrix $\mathbf{R}_i$:

$$1 = q_{1i}^2 + q_{2i}^2 + q_{3i}^2 + q_{4i}^2 \tag{10}$$

The reference frame of the integrated self-calibrating bundle approach is not uniquely defined by known reference points and should be adjusted as an unconstrained network. The rank defect of the resulting singular system of equations can be removed by including seven additional constraints: 3 translations, 3 rotations, 1 scaling factor, e.g. LUHMANN et al. (2006). The scale was determined by two diagonal reference distances across the target field.

Unknown Parameters

The unknown range camera calibration parameters are the focal length c, the principal point x'_0 and the parameters of the image correction functions $\Delta x'$ (interior orientation parameters) as well as linear, periodic and radial distance correction terms, summarised in ΔD:

$$\Delta D = \Delta D_{lin} + \Delta D_{cyc} + \Delta D_{x'y'} \tag{11}$$

They can be estimated from the observation equations (7) and (9). Reflectance dependencies cannot be modelled reliably due to the use of white spheres as reference objects.

Further, exterior orientation parameters $\mathbf{X}_{0i}$ and $(q_1,q_2,q_3,q_4)_i$ for camera translations and rotations as well as all 3D sphere centres $\mathbf{X}_j$ need to be determined in the integrated bundle adjustment. The sphere radius r is introduced as a constant.

4.3 *Stochastic Model*

The stochastic model contains information about the accuracy of the functional model, especially the weighting of the observations. It is represented by the variance-covariance matrix $\mathbf{\Sigma}_{ll}$ of the observations before the adjustment process. Datasets with different types of observations should be separated into groups, and weights should be adjusted in order to tap the full information potential. Usually, information from the instrument manufacturer or from previous accuracy analyses provide the basis for specifying the a-priori variance of a measurement.

The integrated calibration method combines heterogeneous observations with unknown accuracy. The a-priori variance components are adjusted automatically by iterative variance component estimation (VCE). The weights of the observations are given by the quotient of s_0^2 to s_i^2. The variance of the unit weight s_0 is a constant (in general $s_0 = 1$), and s_i are the variances of the observations, namely the variance component s_A^2 for the amplitude image point measurements and s_D^2 for the range measurements. WESTFELD & HEMPEL (2008) already show that an aggregation of all observations of one group with one (adaptive) weight is acceptable for a ToF camera. $\mathbf{\Sigma}_{ll}$ can be subdivided into two components, i.e., one component per group of observation:

$$\mathbf{\Sigma}_{ll} = \begin{bmatrix} \mathbf{\Sigma}_A & \mathbf{0} \\ \mathbf{0} & \mathbf{\Sigma}_D \end{bmatrix} = \begin{bmatrix} s_A^2\mathbf{I} & \mathbf{0} \\ \mathbf{0} & s_D^2\mathbf{I} \end{bmatrix} \tag{12}$$

where $\mathbf{I}$: Identity matrix

In the course of the VCE, the approximate values for the variance components are improved within a few iterations. See KOCH (2004) for further information. The remaining additional constraints are considered to be mathematically rigorous by $\mathbf{P}_C = \mathbf{0}$ in the extended system of normal equations (SNOW 2002, section 4.4).

4.4 *Solving the Adjustment Task*

The integrated bundle adjustment bases on an extended Gauß-Markov model:

$$\mathbf{A\hat{x}} - \mathbf{l} = \mathbf{v}; \qquad \mathbf{B\hat{x}} + \mathbf{w} = \mathbf{0}$$
$$\mathbf{v}^{\mathrm{T}}\mathbf{Pv} + 2\mathbf{k}\left(\mathbf{B\hat{x}} + \mathbf{w}\right) \rightarrow \min \qquad (13)$$
$$\begin{bmatrix} \mathbf{\hat{x}} \\ \mathbf{k} \end{bmatrix} = \begin{bmatrix} \mathbf{A}^{\mathrm{T}}\mathbf{PA} & \mathbf{B}^{\mathrm{T}} \\ \mathbf{B} & -\mathbf{P}_C^{-1} \end{bmatrix} = \begin{bmatrix} \mathbf{A}^{\mathrm{T}}\mathbf{Pl} \\ \mathbf{w} \end{bmatrix}$$

where $\mathbf{v}$: Residuals
           $\mathbf{k}$: Lagrangian multipliers

The functional model (section 4.2) is required to set up the coefficient matrices $\mathbf{A}$ and $\mathbf{B}$, which contain the linearised observation and constraint equations, the reduced observation vector $\mathbf{l}$ and the vector of inconsistencies $\mathbf{w}$. The weight matrix $\mathbf{P}$ as inverse variance-covariance matrix $\mathbf{\Sigma}_{ll}$ defines the stochastic model (section 4.3). The extended system of normal equations is solved iteratively. At each step, the solution vector $\mathbf{\hat{x}}$ is added to the approximation values of the previous iteration until the variances reach a minimum and the optimisation criterion is fulfilled.

As a least squares adjustment method, the integrated bundle adjustment delivers information on the precision, determinability and reliability of the calibration parameters. This includes the a-posteriori variance $\hat{s}_i$ of each of the parameters as well as the correlation between parameters. In combination with an automatic VCE, a-posteriori variances $\hat{s}_l$ and $\hat{s}_{\bar{l}}$ of the original and adjusted observations can be stated.

The ratio between the a-posteriori standard deviation $\hat{s}_{vi}$ of the residuals and the actual residual $\hat{v}_i$ of an observation serves as reliability measure. Per group, the observation with the largest normalised residual above a pre-set threshold is rejected, and the adjustment is repeated until no gross error remains (data snooping).

A student test is calculated after the solution converges to decide whether an introduced parameter is significant or not. Non-significant parameters may be excluded from the estimation process in order to improve the strength of the solution. The least squares adjustment is repeated until all used parameters are significant.

5   **Results**

5.1 *Experimental Setup*

A 1 m² rigid 3D calibration target field was designed in order to proof the concept presented here (Fig. 5). It consists of 25 white polystyrene spheres with a radius r of 35 mm, aligned in two depth planes. The spatial point field with roughly known geometry was captured by a PMD[vision]® CamCube 2.0 (Fig. 6, focal length 12.8 mm, field of view 40° × 40°) following the imaging configuration shown in Fig. 7. The integration time was set to 2,000 µs. The modulation frequency was set to 20 MHz, which corresponds to a non-ambiguous measurement range of 7.5 m. Overall 12 convergent images, four of them rolled against the camera axis, ensure improved ray intersections and lower parameter correlations. A further four camera positions in distances of up to 5 m allow for the determination of distance-related correction terms. Images in larger distances cannot be oriented reliably.

5.2 *Internal Accuracy*

Calibration Parameters

Tab. 1 lists the interior orientation parameters and the corresponding a-posteriori standard deviations. All parameters could be determined significantly, except for the radial distortion parameters A_2 and A_3. Tab. 1 further lists the distance correction terms, and Fig. 8 shows their influence depending on sensor position and distance value. The additive term d_0 of ΔD_{lin} is 115 mm, the multiplicative param-
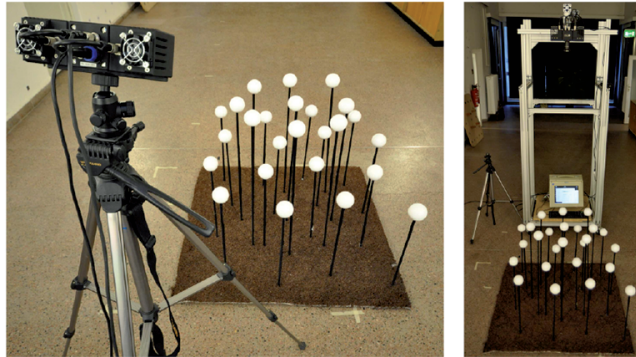
Fig. 5: Target field.
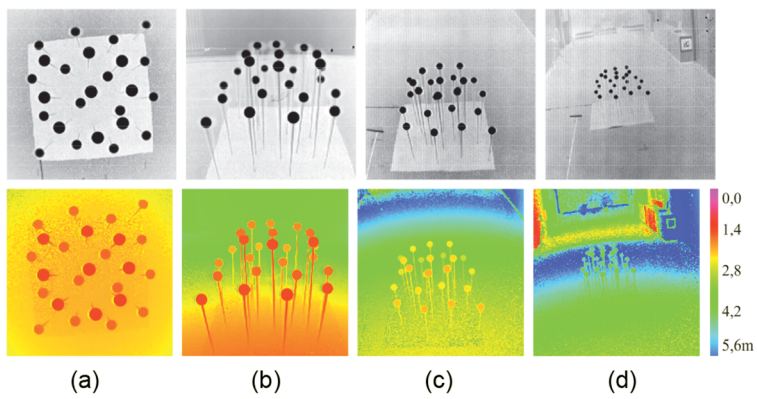

(a)   (b)   (c)   (d)

Fig. 6: Inverse amplitude images (top) und colour-coded range images (bottom) as input data. (a) Frontal view. (b – d) Oblique views at a distance of 1.5 m to 4.5 m.
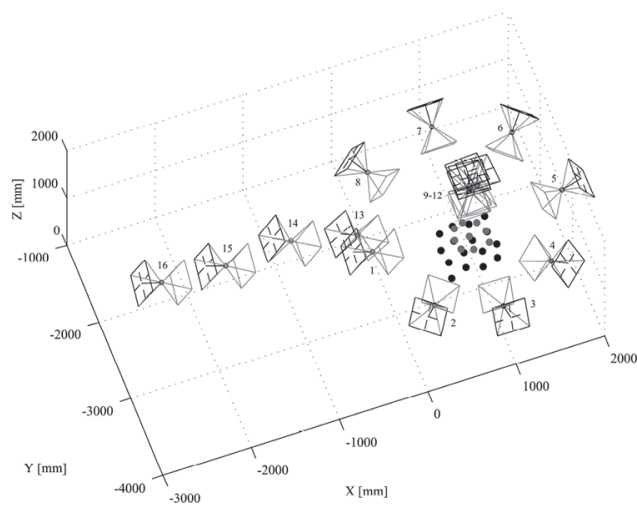

Fig. 7: Network geometry.

Tab. 1: ToF camera calibration parameters $\hat{x}_i$ with their standard deviations $\hat{s}_{\hat{x}_i}$.

	c (mm)	x_0' (mm)	y_0' (mm)	A_1	A_2	A_3	B_1	B_2	C_1	C_2
$\hat{x}_i$	12.149	-0.151	-0.258	-2.85e-3	0	0	3.55e-4	7.02e-4	7.26e-4	-2.32e-4
$\hat{s}_{\hat{x}_i}$	6.48e-3	8.97e-3	8.59e-3	1.29e-5	fix	fix	2.38e-5	2.38e-5	8.78e-5	6.90e-5

	d_0 (mm)	d_1	d_2 (mm)	d_3 (mm)	d_4 (mm)	d_5 (mm)	d_6
$\hat{x}_i$	-115.82	2.88e-2	-33.18	23.98	-8.56	-2.89	3.17
$\hat{s}_{\hat{x}_i}$	15.38	6.33e-3	5.31	4.44	2.09	1.04	0.32

eter d_1 amounts to 2.8 % of the measured distance. The amplitudes $d_{[2,5]}$ of the sinusoidal correction function ΔD_{cyc} show about ±45 mm wave deflection in maximum. The radial factor d_6 in of $\Delta D_{x'y'}$ causes a correction of up to 20 mm for distance measurements at the image corners.

The individual a-posteriori standard deviations of all distance correction parameters seem to be quite high. However, an interpretation is difficult due to non-parameterised remaining errors like scattering or reflectance. Reducing the error model to only a linear correction term would increase the internal accuracy by one order of magnitude ($d_0 =$ -94.13 mm ± 1.235 mm; $d_1 =$ -1.29e-2 ± 6.29e-4), but concurrently increase the distance residuals by more than 5 mm.

The not fully parameterised distance error model also results in high correlations of about 0.90 between all distance correction parameters summarised in ΔD_{lin} and ΔD_{cyc}. The correlations between the other parameters were relatively low. Further considerable cor-relations could not be observed. Particularly, no significant correlations between the interior and exterior orientation parameters and the distance correction parameters could be observed. These correlation coefficients range from -0.07 – +0.09 and from -0.13 – +0.10, respectively.

3D Object Coordinates

The a-posteriori standard deviations of the sphere surface points $\mathbf{X}_{jk}$ observed from one camera position is 0.32 mm; with the redundancy the RMS is improved to 0.13 mm for the sphere centre coordinates $\mathbf{X}_j$.

Residuals

The normally distributed residuals v_A of the amplitude image coordinate measurements $\mathbf{x}'_{ij}$ do not show any systematic effect. They vary in both coordinate directions with an a-posteriori RMS deviation $\hat{s}_{v_i}$ about $1/_{40}$ pixel around the expected value $\mu =$ -0.06 μm (Fig. 9a).

(a) (b) (c) (d) (e)
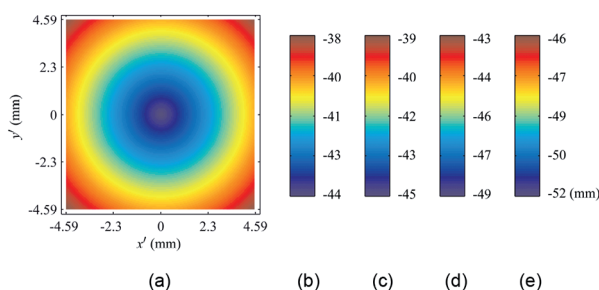
Fig. 8: (a) Effects of the distance correction term on sensor positions, (b) in image distances of 1.0 m, (c) 2.0 m, (d) 3.0 m, and (e) 4.0 m.
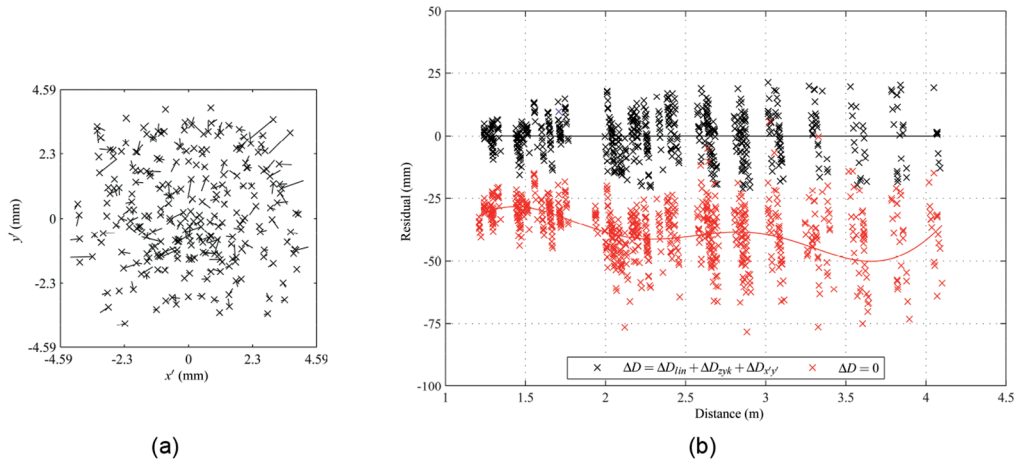
(a)   (b)

Fig. 9: Residuals of the amplitude image coordinate measurements show no systematic effects and are normally distributed around -0.06 µm with an RMS error of $^1/_{40}$ pixel (exaggeration: 200). (b) Residual of the distance measurements without correction show systematic effects (red). The RMS error is 40.86 mm. The residuals do not show interpretable effects, if distance correction terms are included (black). The RMS error can be reduced significantly to 6.49 mm.

The remaining residuals v_D of the distance observations are shown in Fig. 9b for an adjustment with and without considering the distance correction model. The red graph results from of a function fitted into the residuals of the uncorrected distance measurements. It indicates a constant offset, a slight distance-related trend and periodic variations. As expected, the RMS of the residuals is at a height of 40.86 mm. The deviations can be reduced significantly, if distance correction terms are estimated and added. The black graph of a function fitted into the remaining residuals after a fully parameterised adjustment is nearly a straight line with $y = 0$ = const. This is also confirmed by the normally distributed residuals around the expected value $\mu = 0.65$ mm. The RMS error can be reduced by a factor 6 to 6.49 mm.

Observational Errors

The a-posteriori standard deviations $\hat{s}_{A,D}$, the observations estimated by the VCE as well as the $\hat{s}_{\hat{A},\hat{D}}$ of the adjusted observations were calculated in the course of the error analysis after the bundle adjustment (Tab. 2).

In average, the a-posteriori standard deviation $\hat{s}_A$ of an image coordinate measurement

becomes $^1/_{35}$ pixel, and is thus slightly better than the LSM precision stated in section 4.2. The average deviation of an original distance measurement is about 9.5 mm. This value corresponds to the level of precision determined from repeated measurements in preliminary investigations (HEMPEL 2007). The a-posteriori standard deviation of the unit weight is near to the a-priori constant value $s_0 = 1.0$, which indicates an optimally determined accuracy ratio for both groups of observations. This implies that the a-posteriori variances of the original oberservations are equal to their a-priori variances.

The standard deviations $\hat{s}_{\hat{A}}$ and $\hat{s}_{\hat{D}}$ of the adjusted observations, without any systematic errors, are $^1/_{70}$ pixel for the image coordinate measurement and about 0.8 mm for the distance measurement.

Tab. 2: A-posteriori standard deviations $\hat{s}$ of the original and adjusted observations as well as of the unit weight.

$\hat{s}_A$	$\hat{s}_{\hat{A}}$	$\hat{s}_D$	$\hat{s}_{\hat{D}}$	$\hat{s}_0$
1.23 µm	0.65 µm	9.468 mm	0.794 mm	1.00002

5.3 *External Accuracy*

The remaining random measurement deviations and the observational errors as internal precision measures confirm the correctness of the proposed functional and stochastic contexts, but do not reflect the actual physical measurement accuracy.

Images of the target field, captured by a DSLR Nikon D300 and processed by photogrammetric bundle adjustment, are used to obtain 3D sphere centre coordinates with superior accuracy. Such reference data can be used to specify the absolute or external accuracy of the integrated calibration method proposed. The root-mean-square error of the coordinate differences is $RMS_{\Delta \mathbf{X}}$ = 5.3 mm, the minimum deviation is 0.4 mm, the maximum deviation is 10.7 mm.

5.4 *Comparison of 1- and 2-step Procedures*

In order to evaluate the advantages of the integrated approach, the dataset is processed again on the basis of a 2-step calibration. The amplitude image coordinate measurements are introduced into a bundle adjustment, which is only parameterised by the interior and exterior orientation parameters as well as with the 3D sphere centres. Based on this network geometry, the distance correction terms are estimated afterwards by adjusting the range data. The differences in orientation parameter values as well as their accuracies and correlations are marginal. The distance parameter values vary, but their sum ΔD shows a high degree of correspondence. Only the residual analysis show significant improvements: The RMS deviations $\hat{s}_{A,D}$ of the remaining residuals $v_{A,D}$ decrease by 15 % for the integrated approach, and the expected values tend more clearly towards zero. Finally, the RMS of the coordinate differences $\Delta \mathbf{X}$ can be improved slightly by 5 % and thus confirm that the integrated bundle adjustment approach is better suited to model the geometric-physical reality of ToF range imaging process.

A detailed comparison of the three different self-calibration methods for range cameras and the advantages of an integrated self-calibration method in particular are discussed in LICHTI & KIM (2011).

6   **Conclusion and Outlook**

The self-calibrating bundle adjustment approach presented in this contribution determines a geometric range camera model and estimates all image- and distance-related correction parameters. The parameterisation combines both amplitude and distance measurements in an integrated functional model. The heterogeneous information pool is fully exploited by estimating variance components automatically within the integrated stochastic model. The experimental configuration of the self-calibration is based on a small, portable target field, whose geometry is determined simultaneously in the adjustment. Complex experimental set-ups can thus be avoided. The process validation showed that the integration of complementary data leads to a more accurate solution than a 2-step calibration. The RMS error of a 3D coordinate can be stated with 5 mm after the calibration.

Future work can concentrate on an improved experimental setup with grey-scale reference spheres in order to model the dependence of the distance measurements on reflectance. The integration time has an influence on the distance measurements, too. Thus, the calibration should be performed for different integration times. In order to define the scale, two bars of known length, each with two spheres at both ends, can be used as a flexible reference length in object space. As soon as effects of remaining error sources such as scattering are investigated in a strict geometric-physical manner, the parameterisation of the distance correction model can be adapted. To differentiate between constant and distance-related measurement errors, the integration of adaptive variance components is also possible. Finally, the temporal stability of the calibration parameters should be examined and a comparison of different range camera devices should be carried out.

References

ACKERMANN, F., 1984: High precision digital image correlation. – 39th Photogrammetric Week **9:** 231–243, Schriftenreihe der Universität Stuttgart.

BEDER, C. & KOCH, R., 2008: Calibration of focal length and 3D pose based on the reflectance and depth image of a planar object. – International Journal of Intelligent Systems Technologies and Applications **5** (3/4): 285–294.

BÖHM, J. & PATTINSON, T., 2010: Accuracy of exterior orientation for a range camera. – MILLS, J.P., BARBER, D.M., MILLER, P. & NEWTON, I. (eds.): ISPRS Commission V Mid-Term Symposium 'Close Range Image Measurement Techniques' **XXXVIII:** 103–108.

BROWN, D.C., 1971: Close-range camera calibration. – Photogrammetric Engineering **37** (8): 855–866.

BURKHART, S., 2007: Automatische Messung kreisförmiger Zielmarken. – Unveröffentlichte Studienarbeit, Technische Universität Dresden, Institut für Photogrammetrie und Fernerkundung.

CHIABRANDO, F., CHIABRANDO, R., PIATTI, D. & RINAUDO, F., 2009: Sensors for 3D imaging: Metric evaluation and calibration of a CCD/CMOS time-of-flight camera. – Sensors **9** (12): 80–96.

EL-HAKIM, S., 1986: A real-time system for object measurement with CCD cameras. – IAPRS **26**.

FISCHLER, M.A. & BOLLES, R.C., 1981: Random sample consensus: A paradigm for model fitting with applications to image analysis and automated cartography. – Communications of ACM **24** (6): 381–395.

FUCHS, S. & HIRZINGER, G., 2008: Extrinsic and depth calibration of ToF-cameras. – IEEE Conference on Computer Vision and Pattern Recognition (CVPR) **2008:** 1–6.

GRÜN, A., 1985: Adaptive least squares correlation – a powerful image matching technique. – South African Journal of Photogrammetry, Remote Sensing and Cartography **14:** 175–187.

HEMPEL, M., 2007: Validierung der Genauigkeit und des Einsatzpotentials einer distanzmessenden Kamera. – Unveröffentlichte Diplomarbeit, Technische Universität Dresden, Institut für Photogrammetrie und Fernerkundung.

JÄHNE, B., 2002: Digitale Bildverarbeitung. – 5. Auflage, Springer-Verlag, Berlin und Heidelberg.

KAHLMANN, T., REMONDINO, F. & INGENSAND, H., 2006: Calibration for increased accuracy of the range imaging camera swissrangertm. – MAAS, H.-G. & SCHNEIDER, D. (eds.): ISPRS Image Engineering and Vision Metrology **XXXVI** (5): 136–141, ISSN 1682-1750.

KAREL, W., 2008: Integrated range camera calibration using image sequences from hand-held operation. – International Archives of Photogrammetry, Remote Sensing and Spatial Information Sciences **XXXVII:** 945–951.

KAREL, W. & PFEIFER, N., 2009: Range camera calibration based on image sequences and dense, comprehensive error statistics. – BERALDIN, A., CHEOK, G.S., MCCARTHY, M. & NEUSCHAEFER-RUBE, U. (eds.): SPIE Proceedings on Electronic Imaging / 3D Imaging Metrology **7239**, San José, CA, USA.

KAREL, W., GHUFFAR, S. & PFEIFER, N., 2012: Modelling and compensating internal light scattering in time of flight range cameras. – Photogrammetric Record **27:** 155–174.

KOCH, K.-R., 2004: Parameterschätzung und Hypothesentests in linearen Modellen. – 4. Auflage, Dümmlers Verlag, Bonn.

KOLB, A., BARTH, E., KOCH, R. & LARSEN, R., 2010: Time-of-flight cameras in computer graphics. – Computer Graphics, Forum **29** (1): 141–159.

LICHTI, D.D., KIM, C. & JAMTSH, S., 2010: An integrated bundle adjustment approach to range camera geometric self-calibration. – ISPRS Journal of Photogrammetry and Remote Sensing **65** (4): 360–368.

LICHTI, D.D. & KIM, C., 2011: A Comparison of Three Geometric Self-Calibration Methods for Range Cameras. – Remote Sensing **3:** 1014–1028.

LICHTI, D.D., QI, X. & AHMED, T., 2012: Range camera self-calibration with scattering compensation. – ISPRS Journal of Photogrammetry and Remote Sensing **74:** 101–109.

LICHTI, D.D. & QI, X., 2012: Range camera self-calibration with independent object space scale observations. – Journal of Spatial Science **57** (2): 247–257.

LINDNER, M. & KOLB, A., 2009: Compensation of Motion Artifacts for Time-of-Flight Cameras. – Dynamic 3D Imaging, LNCS: 16–27, Springer.

LUAN, X., 2001: Experimental Investigation of Photonic Mixer Device and Development of TOF 3D Ranging Systems Based on PMD Technology. – Dissertation, Department of Electrical Engineering and Computer Science, Universität Siegen.

LUHMANN, T., ROBSON, S., KYLE, S. & HARLEY, I., 2006: Close Range Photogrammetry: Principles, Methods and Applications. – Whittles Publishing, revised edition.

MÖNNICH, H., NICOLAI, P., BEYL, T., RACZKOWSKY, J. & WÖRN, H., 2011: A supervision system for the intuitive usage of a telemanipulated surgical robotic. – IEEE International Conference on Ro-

botics and Biomimetics (ROBIO 2011): 449–454.

MURE-DUBOIS, J. & HÜGLI, H., 2007: Real-time scattering compensation for time-of-flight camera. – 5th International Conference on Computer Vision Systems.

REICH, M., 2011: Untersuchung des Einsatzpotentials einer Laufzeitkamera zur quantitativen Erfassung von Verkehrsströmen. – Studienarbeit, Technische Universität Dresden, Institut für Festkörperelektronik.

REULKE, R., 2006: Combination of distance data with high resolution images. – ISPRS Commission V Symposium.

RINGBECK, T. & HAGEBEUKER, B., 2007: Dreidimensionale Objekterfassung in Echtzeit – PMD Kameras erfassen pro Pixel Distanz und Helligkeit mit Videoframerate. – Allgemeine Vermessungs-Nachrichten **114** (7): 263–270.

RINGBECK, T., MÖLLER, T. & HAGEBEUKER, B., 2007: Multidimensional measurement by using 3-D PMD sensors. – Advances in Radio Science **5:** 135–146.

ROBBINS, S., MURAWSKI, B. & SCHRÖDER, B., 2009: Photogrammetric calibration and colorization of the swissranger SR-3100 3-D range imaging sensor. – Optical Engineering **48:** 053603–053603–8.

SCHULZE, M., 2010: 3D-camera based navigation of a mobile robot in an agricultural environment. – MILLS, J.P., BARBER, D.M., MILLER, P. & NEWTON, I. (eds.): The International Archives of the Photogrammetry, Remote Sensing and Spatial Information Sciences **XXXVIII:** 538–542.

SCHWARTE, R., 1996: Eine neuartige 3D-Kamera auf der Basis eines 2D-Gegentaktkorrelator-Arrays. – Aktuelle Entwicklungen und industrieller Einsatz der Bildverarbeitung: 111–117, Aachen, MIT GmbH.

SCHWARTE, R., HEINOL, H., BUXBAUM, B., RINGBECK, T., XU, Z. & HARTMANN, K., 1999: Principles of three-dimensional imaging techniques. – JÄHNE, B., HAUSSECKER, H. & GEISSLER, P. (eds.): Handbook of Computer Vision and Applications – Sensors and Imaging **1** (18): 463–484, Academic Press.

SNOW, K.B., 2002: Applications of Parameter Estimation and Hypothesis Testing of GPS Network Adjustments. – Technical Report 465, Geodetic and GeoInformation Science, Department of Civil Environmental Engineering and Geodetic Science, The Ohio State University, Columbus, Ohio, USA.

SPIRIG, T., SEITZ, P., VIETZE, O. & HEITGER, F., 1995: The lock-in CCD-two-dimensional synchronous detection of light. – IEEE Journal of Quantum Electronics **31** (9): 1705–1708.

WESTFELD, P., 2007: Ansätze zur Kalibrierung des Range-Imaging-Sensors SR-3000 unter simultaner Verwendung von Intensitäts- und Entfernungsbildern. – LUHMANN, T. (ed.): Photogrammetrie – Laserscanning – Optische 3D-Messtechnik (Beiträge Oldenburger 3D-Tage 2007): 137–146, Herbert Wichmann Verlag, Heidelberg.

WESTFELD, P. & HEMPEL, R., 2008: Range image sequence analysis by 2.5-D least squares tracking with variance component estimation and robust variance covariance matrix estimation. – CHEN J., JIANG, J. & MAAS, H.-G. (eds.): International Archives of Photogrammetry, Remote Sensing and Spatial Information Sciences **XXXVII:** 457–462, ISPRS.

WESTFELD, P., MULSOW, C. & SCHULZE, M., 2009: Photogrammetric calibration of range imaging sensors using intensity and range information simultaneously. – Optical 3D Measurement Techniques **IX** (II): pp. 129.

WESTFELD, P., 2012: Geometrische und stochastische Modelle zur Verarbeitung von 3D-Kameradaten am Beispiel menschlicher Bewegungsanalysen. – Dissertation, Technische Universität Dresden, Fakultät Forst-, Geo- und Hydrowissenschaften, Professur für Photogrammetrie.

WESTFELD, P., MAAS, H.-G., BRINGMANN, O., GRÖLLICH, D. & SCHMAUDER, M., 2013: Automatic techniques for 3D reconstruction of critical workplace body postures from range imaging data. – ISPRS Journal of Photogrammetry and Remote Sensing, http://dx.doi.org/10.1016/j.isprsjprs.2013.08.004.

Address of the Authors:

Dr.-Ing. PATRICK WESTFELD, Prof. Dr. sc. techn. habil. HANS-GERD MAAS, Technische Universität Dresden, Institute Photogrammetry and Remote Sensing, D-01062 Dresden, Tel.: +49-351-463-39701, Fax: +49-351-463-37266, e-mail: {patrick.westfeld}{hans-gerd.maas}@tu-dresden.de